Synergistic Tuning of Nickel Cobalt Selenide@Nickel Telluride Core–Shell Heteroarchitectures for Boosting Overall Urea Electrooxidation and Electrochemical Supercapattery

Diab Khalafallah* , Weibo Huang, Mingjia Zhi* , and Zhanglian Hong*

Herein, we demonstrate the synthesis of bifunctional nickel cobalt selenide@nickel telluride ($Ni_xCo_{12-x}Se@NiTe$) core–shell heterostructures via an electrodeposition approach for overall urea electrolysis and supercapacitors. The 3D vertically orientated NiTe dendritic frameworks induce the homogeneous nucleation of 2D $Ni_xCo_{12-x}Se$ nanosheet arrays along similar crystal directions and bring a strong interfacial binding between the integrated active components. In particular, the optimized $Ni_6Co_6Se@NiTe$ with an interface coupling effect works in concert to tune the intrinsic activity. It only needs a low overpotential of 1.33 V to yield a current density of 10 mA cm^{-2} for alkaline urea electrolysis. Meanwhile, the full urea catalysis driven only by $Ni_6Co_6Se@NiTe$ achieves 10 mA cm^{-2} at a potential of 1.38 V and can approach a constant level of the current response for 40 h. Besides, the integrated $Ni_6Co_6Se@NiTe$ electrode delivers an enhanced specific capacity (223 mA h g^{-1} at 1 A g^{-1}) with a high cycling stability. Consequently, a hybrid asymmetric supercapacitor (HASC) device based on $Ni_6Co_6Se@NiTe$ exhibits a favorable rate capability and reaches a high energy density of 67.7 Wh kg^{-1} and a power density of 724.8 W kg^{-1} with an exceptional capacity retention of 92.4% after sequential 12 000 cycles at 5 A g^{-1}.

1. Introduction

The urgency in eco-benign and sustainable energy conversion and storage technologies as alternatives to nonrenewable fossil fuels have collectively triggered numerous efforts to explore suitable electroactive materials with desirable compositional and architectural advantages.[1–4] In fact, the majority of ongoing energy systems are mainly dominated by traditional fossil fuels, which cause many harmful impacts and global climate change, thereby establishing green energy systems becomes a key pillar to the nations and economic development. In the present scenario, electrochemical energy appliances represent the next-generation energy devices and can drive the substantial transition from conventional energy sources with multiple merits of renewability and adequate energy density as well as nontoxicity.[5–7] To date among several technologies, supercapacitors are drawing significant interest in the field of energy storage because of their rapid charge/discharge rates, adaptability to severe environments, and excellent safety.[5,8] Moreover, producing hydrogen (H_2) via an eco-friendly approach holds great promise for our society's future clean energy carriers. In this regard, urea electrocatalysis has experienced an exponential growth as an effective approach to work in synergy for large-scale hydrogen production.[9–11] One of the most efficient strategies to enhance the sustainable energy systems' feasibility and increase their energy/power outputs is to design highly active materials. Therefore, physical geometries, surface properties, elemental compositions, and inherent electrical conductivity must be considered.

The current need for effective bifunctional electrodes/electrocatalysts has inspired the modulation of electroactive materials through versatile aspects such as structural/compositional engineering and heteroatom insertion. Thus, achieving heterostructure interfaces with tunable electronic structures is essential to extensively increase the density of active sites and boost the intrinsic electrocatalytic capability.

Transition metal selenides/tellurides-derived heterostructures have been considered prominent candidates for energy conversion and storage systems due to their versatile crystal structures, enhanced electrochemical activity, excellent redox chemistry, and enhanced electronic conductivity.[12–14] In particular, Ni-Co–based selenides/tellurides have been investigated as electrode/electrocatalyst materials in supercapacitors,[15] batteries,[16] overall water splitting,[17–19] and urea electrooxidation.[10,20] These materials were reported to display decently high activity at affordable cost with advantageous attributes of good reversibility and diverse valence states. Besides, the intercalations of nonmetallic species in metal selenides/tellurides endow superior conductivity than hydroxide or oxide counterparts.[21,22]

Dr. D. Khalafallah, W. Huang, Associate Prof. M. Zhi, Prof. Z. Hong
State Key Laboratory of Silicon Material, School of Materials Science and Engineering, Zhejiang University, 38 Zheda Road, Hangzhou 310027, China
E-mail: diab_khalaf@energy.aswu.edu.eg
E-mail: mingjia_zhi@zju.edu.cn
E-mail: hong_zhanglian@zju.edu.cn
Dr. D. Khalafallah
Mechanical Design and Materials Department, Faculty of Energy Engineering, Aswan University, P.O. Box 81521, Aswan, Egypt
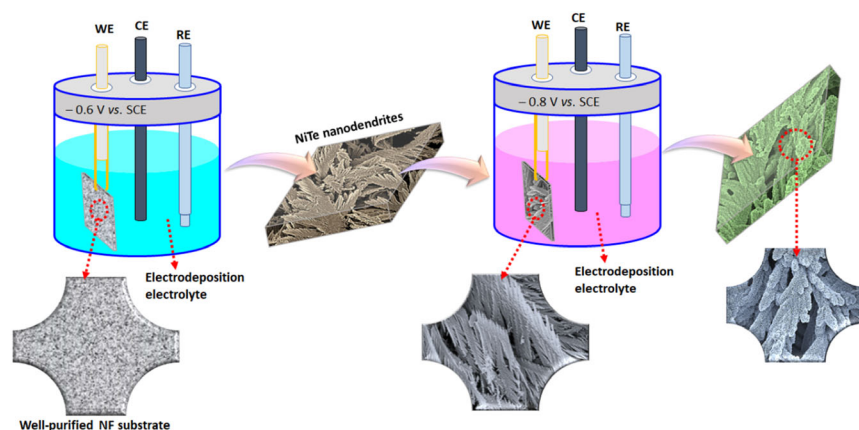ID The ORCID identification number(s) for the author(s) of this article can be found under https://doi.org/10.1002/eem2.12528.

Figure 1. Representative diagram for the synthetic strategy of $Ni_xCo_{12-x}Se@NiTe$ heterostructures via a electrodeposition approach.

2. Results and Discussion

2.1. Morphological Investigation of Hierarchical $Ni_xCo_{12-x}Se@NiTe$ Core–Shell Heterostructures

The direct growth of freestanding $Ni_xCo_{12-x}Se@NiTe$ heterostructures on Ni foam (NF) can be realized via an effective electrodeposition approach (**Figure 1**). As a noticeable contrast with other current collectors, NF attracts the most priority due to its low cost and large conductive scaffold with well-defined macropores. It can be employed as a typical Ni precursor to fabricate Ni-based functional compounds.[6,7] Electrodeposition affords the advantages such as ease of composition control and relatively environmental friendliness. Most importantly, potentiostatic-assisted in situ growth of active components in a single electrolytic solution facilitates the disposition process and reduces the time needed to accomplish the desirable structures at a reasonable rate (Supporting Information Figure S1).

The 2D porous nanosheet@3D dendritic frameworks-like heterostructures with hierarchical assemblies are caused by self-assembly and oriented attachment. When a current passes through an electrolyte of $Ni(NO_3)_2$ and $Co(NO_3)_2$, the generation of OH^- ions can be maximized, which in turn impacts the local pH value, directing the uniform deposition of target material onto the working electrode. Thus, the electrolytic deposition process involves an electrochemical reaction and a subsequent precipitation reaction. The hydrolysis equilibrium of metal ions in water supplies OH^- ions to form primary nanocrystals and guide the crystal growth as well as the oriented attachment. In addition, the coordination between metal ions and OH^- plays a considerable role in the assembly and self-attachment of building units.

It can be speculated that the primary crystals are rearranged to produce bunches of side-by-side trunks through oriented attachment to extremely minimize the interfacial energy.[30] After the self-assembly process, the loose dendrites become compact gradually along a single crystallographic orientation owing to Ostwald ripening effect. Accordingly, the individual dendritic architecture regulates to illustrate the shape of single crystals. Subsequently, the 2D nanosheets are completely anchored on the dendritic arrays of the NiTe core, constructing hierarchical complex heterostructures, manifesting that the oriented attachment mechanism represents a major path for the achievement of $Ni_xCo_{12-x}Se@NiTe$ heterostructures.

The morphologies of $Ni_xCo_{12-x}Se@NiTe$ heterostructures are characterized by a field emission scanning electron microscope (FE-SEM). As displayed in **Figure 2**a1–a3 and Supporting Information Figure S2A,B, the SEM micrographs of pure NiTe electrode show 3D dendritic arrays with a compact and dense morphological yield. Representative observations unambiguously reveal that the fractal structure of each dendritic scaffold is featured with side nanohyperbranches slitting from the main trunk, similar to the tree branches of metasequoia. Such morphology can expose plentiful electroactive centers for electrolyte and reactants. With tunable Ni/Co ratios, the $Ni_4Co_8Se@NiTe$ (Figure 2b1–b3; Supporting Information Figure S2C,D), $Ni_6Co_6Se@NiTe$ (Figure 2c1–c3; Supporting Information Figure S2E,F), and $Ni_8Co_4Se@NiTe$ (Figure 2d1–d3; Supporting Information Figure S2G,H) samples illustrate
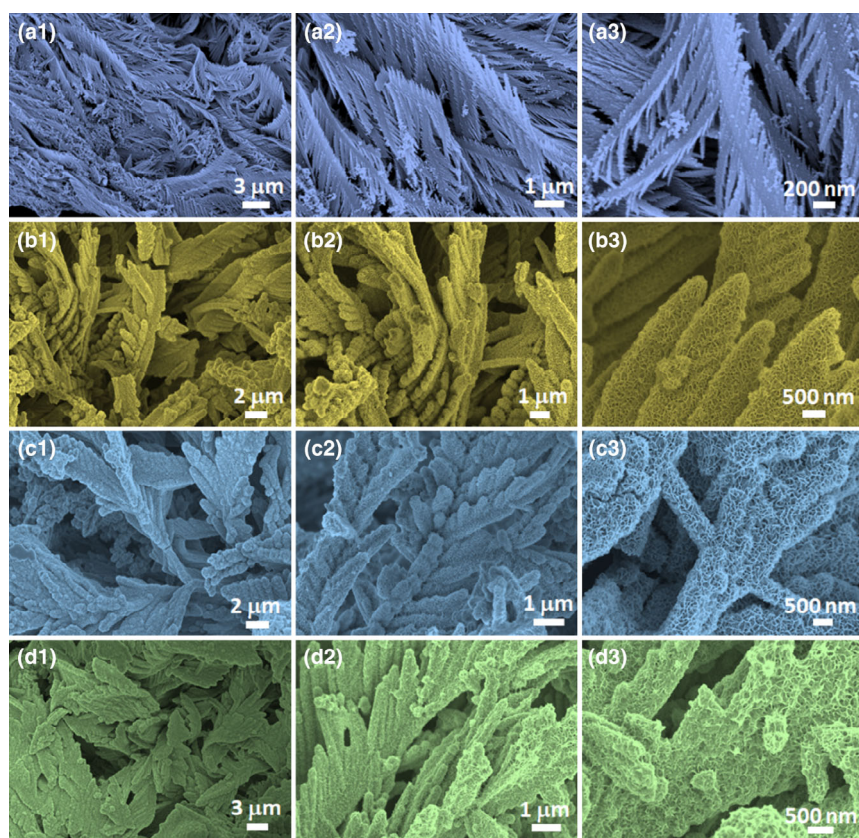
In general, the rational construction of benefit-enriched architectures with exceptional porosity can greatly facilitate the shortage of ion diffusion lengths by minimizing the active compounds' intrinsic resistance. Nanoscale frameworks with multiple open spaces not only maximize the contact area with electrolyte ions but also expose numerous active sites and trigger rapid electrochemical reactions.[23,24] Moreover, developing core–shell-like hybrid architectures combining dual metal active components and in situ heteroatoms dopants within the host material can significantly regulate the electronic state, improve the intrinsic conductivity, and mitigate the drawbacks of metal chalcogenides in their solitary form.[25,26] Synergistic core–shell-based heterostructures offer elastic charge transportation pathways into both shell and core regions and possess the advantage of each component. Thus, effectively contributing to the enhanced energy conversion/storage capability. Additionally, engineering a heterojunction and multi-metallization to establish an interface coupling effect can accelerate the breakage of chemical bonds and accelerate the charge transfer rate. The heterogeneous interface between various compositions upregulates the density of active sites, tunes the electronic interaction, and promotes the adsorption of reactants and electrolyte molecules onto active centers, enabling better electrochemical activity.[27–29]

Herein, we propose hierarchical $Ni_xCo_{12-x}Se@NiTe$ core–shell heterostructures with many compositional and architectural advantages for electrocatalytic UOR and supercapacitor applications. The porous network-like 2D-arrayed nanosheets-coated 3D dendritic frameworks expose more accessible active sites and facilitate the mass/electron penetration for enhanced electrooxidation reactions and rapid Faradic redox processes. $Ni_xCo_{12-x}Se$ as an electroactive shell can enlarge the surface area and contribute to the majority of the electrocatalytic and capacitive effects. The NiTe dendritic frameworks serve as a robust core scaffold to fasten ion diffusion and electron transport as well as maintain the structure stability by controlling the volume expansion and contraction. Benefiting from the favorable synergistic effect, the overall urea−water electrolyzer ($Ni_6Co_6Se@NiTe \parallel Ni_6Co_6Se@NiTe$) achieves an enhanced electrocatalytic performance in terms of low cell voltage and long-term durability. In view of the outstanding pseudocapacitance, the as-assembled $Ni_6Co_6Se@NiTe$//activated carbon (AC) HASC device realizes high energy storage performance and competitive energy/power outcomes together with improved cycle stability.

Figure 2. Field emission scanning electron microscope images of $Ni_xCo_{12-x}Se@NiTe$ core–shell heterostructures. a1–a3) NiTe, b1–b3) $Ni_4Co_8Se@NiTe$, c1–c3) $Ni_6Co_6Se@NiTe$, and d1–d3) $Ni_8Co_4Se@NiTe$.

a high and uniform coverage of squama-like architectures consisting of 2D $Ni_xCo_{12-x}Se$ nanosheet network on the surface of freestanding NiTe dendritic frameworks, suggesting the formation of core–shell-like intercalated hybrids. Obviously, the cross-linked nanosheets are vertically anchored on epitaxially grown dendritic arrays, resulting in unique hierarchical heterostructures with a wide range of void spaces and pores. The wrinkled nanosheets are tightly clumped together without agglomerations, producing interconnecting and channel-opening architectures.

The representative SEM–EDX mapping profiles of samples (Supporting Information Figures S3–S6) elucidate the coexistence and homogeneous distribution of Ni, Co, Te, and Se components throughout the synthesized materials. The core–shell heterostructures can provide a large electrochemically active surface area, rich paths for effective charge transport/ion penetration, and expose more edges for electrochemical reactions. These characteristics may tune the kinetics of both electrooxidation processes and Faradaic redox reactions.

To interpret the structural information of as-formed $Ni_xCo_{12-x}Se@NiTe$ samples, XRD measurements are conducted. The patterns of bare NF and pure NiTe are also acquired for comparison (**Figure 3**a). Clearly, the diffraction signs observed at 44.9, 52.3, and 76.7° are mainly associated with the (111), (200), and (220) planes of metallic Ni, respectively (PDF no. 04–0850). The diffraction peaks of telluride-based samples can be ascribed to the hexagonal NiTe phase (PDF no. 38–1393) with P63/mmc space group. The corresponding peaks

located at 26, 31.1, 42.6, 58.2, and 64.7° are assigned to (100), (101), (102), (103), and (202) planes of NiTe, respectively.

$Ni_6Co_6Se@NiTe$ core–shell hybrid was investigated as a representative sample for further characterization because of its superior electrochemical behavior among all designed electrodes. To further probe the composition and oxidation states of the $Ni_6Co_6Se@NiTe$ hybrid, XPS measurements were performed to analyze the near-surface properties. Figure 3b shows the XPS survey spectrum with the coexistence of Ni 2p, Co 2p, Te 3d, and Se 3d-binding energies. The Ni 2p core-level (Figure 3c) reveals two peak doublets, which correlate with Ni $2p_{3/2}$ (855.3/872.9 eV), Ni $2p_{1/2}$ (856.5/874.1 eV), and their corresponding shakeup satellite components (denoted as "Sat.", 861.3/879.5 eV).[20,31] These findings confirm the occurrence of Ni^{2+}- and Ni^{3+}-oxidized states of Ni. Similarly, the high-resolution Co 2p XPS spectrum (Figure 3d) exhibits two major bands related to Co $2p_{3/2}$ and Co $2p_{1/2}$ characteristics. Each band can be fitted with two subpeaks. Co^{3+} $2p_{3/2}$ and Co^{3+} $2p_{1/2}$ can be identified at 776 and 790.2 eV, whereas the positions of Co^{2+} $2p_{3/2}$ and Co^{2+} $2p_{1/2}$ are located at 780.8 and 796.2, respectively.[20,31] Besides, the satellite shoulders are centered at 784.2 and 801.7 eV. In the case of the Te 3d spectrum, the peaks at binding energies of 573 and ~583.5 eV are mainly related to Te $3d_{5/2}$ peaks and Te $3d_{3/2}$, respectively, suggesting the occurrence of Te^{2-} oxidation state inside the sample (Figure 3e). On the other hand, the satellite signals positioned at ~576 and 586.3 eV originate from the trace surface oxidation. Moreover, the deconvolution of Se 3d spectrum (Figure 3f) presents two peaks at 56.8 and 57.9 eV attributed to Se $3d_{5/2}$ and Se $3d_{3/2}$, respectively. This validates the existence of Se^{2-} and metal-Se bonds.[32,33] The remaining peaks at 58.4 and 59 eV are ascribed to SeO_x caused by superficial oxidations.[32,33]

To further explore the microstructure of porous hierarchical $Ni_6Co_6Se@NiTe$ core–shell heterostructures. Transmission electron microscopy (TEM), high-resolution TEM (HR-TEM), high-angle annular dark-field scanning TEM (S-TEM), and corresponding energy-dispersive spectroscopy (EDS) characterizations were also conducted. Low-magnification TEM images demonstrate a frame-like core–shell structure, in which the surfaces of arrayed dendrites are fully decorated with many slightly wrinkled and radially arranged nanosheets (**Figure 4**a,b; Supporting Information Figure S7). The interlacing between the 3D-arrayed dendrites and the 2D nanosheet constructs a hierarchical core–shell architecture with smart characteristics. Interestingly, there is an incoherent interface between the Ni_6Co_6Se shell and NiTe core, which demonstrates sturdy evidence that the arrayed dendrites may serve as propitious sites for the heterogeneous nucleation of 2D porous nanosheets (Figure 4c). A clear central branch with hierarchically leaves (tertiary branch) is illustrated in Figure 4d (marked by the white dotted lines). The multilevel branches preferentially grow along specific directions with respect to their corresponding central backbone. Such special
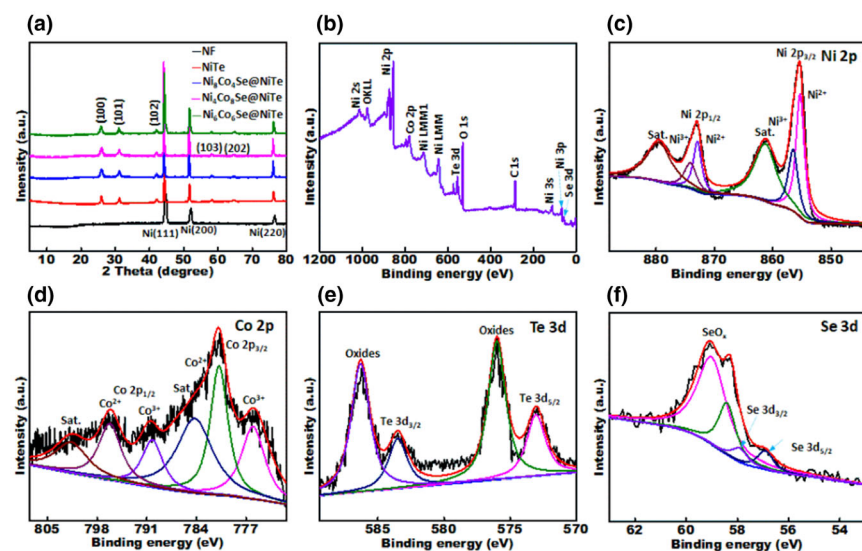
Figure 3. a) XRD patterns of bare NF, pure NiTe, and $Ni_xCo_{12-x}Se@NiTe$ core–shell hybrids, b) XPS survey scan, and corresponding deconvoluted spectrum for c) Ni 2p, d) Co 2p, e) Te 3d, and f) Se 3d core level of hierarchical porous $Ni_6Co_6Se@NiTe$ hybrid.

morphology indicates that the 3D NiTe dendritic arrays grow along a preferential direction.

Moreover, HR-TEM results present the occurrence of crystal/local lattice distortions (indicated by the red dotted circles—Figure 4e,f), which are ascribed to the slight change in prioritized crystal growth plane of secondary/tertiary branches on both sides of the trunk (trunk in the center with two rows of secondary branches growing on both sides) with respect to the growth direction of the central trunk of a dendritic particle.[34] The residual stress induced by interface defects and heterogeneous nucleation or hybridization can cause changes in the degree of crystallinity of NiTe. Besides, the partial substitution of Ni with Co atoms around the heterointerface regions stimulates the formation of disordered phases and structural defects.[35] No clear crystal lattices can be discerned within the surface of the shell layer, manifesting that the Ni_6Co_6Se nanosheets are in an amorphous phase (Figure 4e,f), consistent with the XRD results.

High-resolution TEM analysis shows that the NiTe core and Ni_6Co_6Se shell are inextricably neighboring each other, revealing the formation of closely contacted heterointerfaces throughout the entire architecture and the boundaries are identified by green dashed lines (Figure 4e,f). Distinctly, the observed lattice fringes in the HR-TEM images (Figure 4e,f) with a distance of 0.25 and 0.32 nm are related to the (101) and (100) planes, respectively, of NiTe. The distribution of Ni, Co, Te, and Se elements inside the hybrid is further verified by EDS-mapping profiles. Figure 4g confirms the coexistence of all four components with a homogenous distribution throughout the entire structure. Results elucidate that the Co and Se species exhibit a similar distribution feature as Ni and Te, which strongly evidences the construction of intimately connected heterointerfaces because the inner core offers abundant growth centers for the heterogeneous nucleation of the outer shell. Generally, such hierarchical 2D nanosheet arrays-on-3D dendritic frameworks with additional defects and many heterointerfaces can expand the contact area between the electrolyte and active material, supply more electroactive sites, establish accessible electron/

ion transport pathways, and regulate the intrinsic electrical conductivity and wettability.

2.2. UOR Electrocatalytic Activity of $Ni_xCo_{12-x}Se@NiTe$ Heterosuperstructures

Urea molecule with a satisfactory thermodynamic oxidation potential is an optimal candidate for energy-efficient generation of hydrogen. To explore the catalytic effect of multiple synergistic systems, the electrocatalytic performance of pure NiTe and heterostructured $Ni_xCo_{12-x}Se@NiTe$ core–shell electrodes for UOR was evaluated in 1.0 M KOH solution with 0.5 M urea at room temperature by using a typical three-electrode cell. **Figure 5a** presents the linear sweep voltammetry (LSV) curves at a scan rate of 5 mV s^{-1}, in which the optimized $Ni_6Co_6Se@NiTe$ electrode reveals a greatly enhanced electrocatalytic activity with a higher anodic current density. Consequently, the dramatic increase in UOR electrocatalytic activity can result from the synergistic effect of the 3D core-like NiTe shelled with 2D $Ni_xCo_{12-x}Se$ nanosheets, which boosts the ultrafast migration of ions into the whole system. As observed, the $Ni_6Co_6Se@NiTe$ electrode achieves a current density of 10 mA cm^{-2} at a potential of 1.33 V, which is lower than that of $Ni_4Co_8Se@NiTe$ (1.35 V), $Ni_8Co_4Se@NiTe$ (1.36 V), NiTe (1.36 V), RuO_2 (1.37 V), and bare NF (1.51 V). As can be seen in the plotted histogram (Figure 5b), $Ni_6Co_6Se@NiTe$ requires an inferior overpotential to realize a high current density among the other electrodes. Accordingly, the $Ni_6Co_6Se@NiTe$ electrode can reach a higher current density of 100 and 400 mA cm^{-2} at a potential of 1.46 and 1.67 V versus RHE, respectively (Figure 5a,b). It is worth that the starting potential of UOR over the $Ni_6Co_6Se@NiTe$ electrode is about ~1.31 V versus RHE, which is very close to the oxidation potential of $Ni^{2+} \rightarrow Ni^{3+}$, proposing that the high-valence Ni^{3+} sites greatly trigger the UOR activity.[36] Reported data claimed that the electrooxidation of urea as a surface-based reaction starts with the adsorption of OH$^-$ ions, converting Ni^{2+} to Ni^{3+} and Co^{2+} to Co^{3+}. Meanwhile, the adsorption of urea takes place through bridging the Ni–O, Co–O, and O–C coordination bonds with NiOOH, manifesting that the Co valence centers contribute to the process. Clearly, the surface-based electrooxidation of urea molecules occurs simultaneously. Incorporating Co species into Ni-based electrocatalysts is preferable to decrease the onset potential and tune the electronegativity of Ni within the system.[37] Thus, Co atoms optimize the electronic structure of constructed heterojunction, expose more active sites, and improve the electrochemical performance. Therefore, the deposition promotes the UOR process due to tunable electronic configuration, and coexistence of multiple electrochemically active sites for effective UOR as a result of the induced atomic defects. Compared to pure NiTe, the $Ni_6Co_6Se@NiTe$ electrode exhibits a significant enhancement in the current density, illustrating that the UOR process can be accelerated by forming an interface engineering between NiTe and $Ni_xCo_{12-x}Se$. The robust electron interactions of $Ni_6Co_6Se@NiTe$ heterostructure may accelerate the formation of Ni^{3+} through losing electrons from the
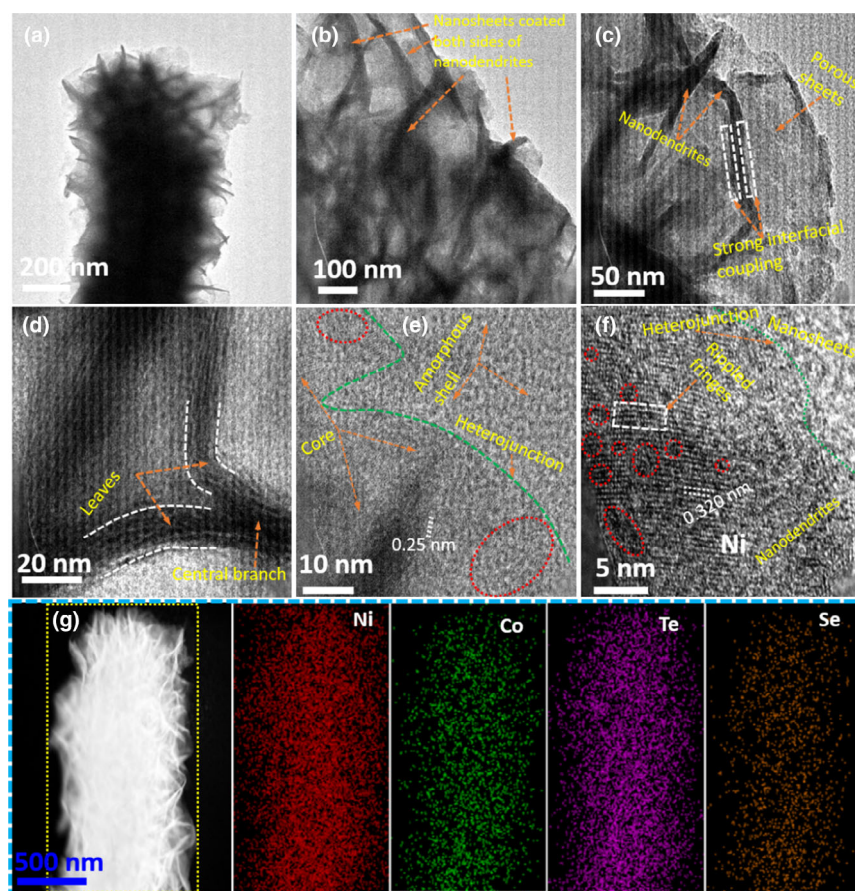
Figure 4. a–c) Low-resolution and magnified transmission electron microscopy (TEM) images of $Ni_6Co_6Se@NiTe$ core–shell hybrid, d–f) high-resolution TEM portraits, and g) scanning TEM image and corresponding energy-dispersive spectroscopy-based elemental mapping analysis for Ni, Co, Te, and Se elements.

$Ni_6Co_6Se@NiTe$ core–shell is mainly caused by the Ni^{2+}/Ni^{3+} and Co^{2+}/Co^{3+} redox transition.[38] Notably, a significant enhancement in the electrocatalytic behavior is evident from the large anodic current density with a potential shift after inserting urea into the alkaline electrolyte (1 M KOH + 0.5 M urea). This observation implies that the UOR requires a lower potential compared to OER.

The intrinsic catalytic area of active materials can be evaluated by the electrochemical surface area (ECSA). The double-layer capacitance (C_{dl}) calculations were performed based on the non-Faradaic potential window. The cyclic voltammetry (CV) curves of pure NiTe and $Ni_xCo_{12-x}Se@NiTe$ electrodes at a scan rate of 10–100 mV s^{-1} are depicted in Supporting Information Figure S8. The $Ni_6Co_6Se@NiTe$ sample has the largest C_{dl} value (Figure 5e), implying that the electrode offers a more effective catalytic area and possesses a wide range of chemically active sites caused by the Ni and Co synergism. The 2D nanosheet@3D dendritic framework heterostructures with copious heterojunctions and multiple channels are useful to enlarge ECSA and promote mass transfer.

To disclose the interfacial transport mechanism and active material intrinsic kinetics for UOR, EIS tests of as-prepared electrodes are implemented in a 1 M KOH electrolyte with 0.5 M urea around the onset potential. Supporting Information Figure S9 presents the corresponding Nyquist plots and suggested equivalent electrical circuit with a solution resistance (R_s), constant phase element (CPE), and charge transfer impedance (R_{ct}). Results demonstrate that constructing a porous shell of Ni, Co, and Se elements can speed up the interface electronic transfer, and hence, the R_{ct} of $Ni_xCo_{12-x}Se@NiTe$ core–shell heterostructures is reduced compared to pure NiTe, suggesting a faster conduction rate. The collaborative effect of both Te and Se species increases the conductivity and utilization efficiency of electrode material. The regulated electric conductivity of the $Ni_xCo_{12-x}Se@NiTe$ core–shell electrode strengthens the electrochemical activity and improves UOR. Apparently, the $Ni_6Co_6Se@NiTe$ displays a smaller R_{ct} (1.92 Ω), validating its low ionic/electronic resistance and reinforced charge transfer rate. Additionally, the intrinsic R_s of pure NiTe and heterostructured $Ni_6Co_6Se@NiTe$ are significantly small (~0.72 Ω). This finding can be recognized by the fact that the vertically grown nanosheets@dendritic arrays are suitable for UOR electrocatalysis because of their close contact with each other and with the current collector as well. This can reduce the resistance and shorten the ion diffusion distances. Hereby, it can be noted that the EIS results are coincident with the analyzed Tafel slopes and potentials of designed electrodes, unambiguously disclosing that the formation of heterojunctions with lattice defects, multiple active sites, and full diffusion of electrolyte ions effectively boosts the UOR kinetics of $Ni_xCo_{12-x}Se@NiTe$.

Durability is an important aspect for assessing the catalytic performance of an electrocatalyst. Herein, the long-term durability of $Ni_6Co_6Se@NiTe$ was characterized by the chronoamperometry tactic (i–t test) at

Ni component, and thereby enabling a good UOR activity. The electrocatalytic activity of $Ni_6Co_6Se@NiTe$ for UOR is comparable or even superior to other non-noble metal catalysts reported in the literature, revealing its impressive potential for practical applications (Supporting Information Table S1).

The UOR kinetics is further explored by the Tafel slope. Figure 5c compares the Tafel slopes of designed electrodes. A smaller Tafel slope implies that a lower potential can be reached at a higher current density, suggesting rapid electron transfer rate and better electrocatalysis properties. The Tafel slope of $Ni_6Co_6Se@NiTe$ is about 36.1 mV dec^{-1}, which is much lower than that of bare NF and slightly lower than that of other $Ni_xCo_{12-x}Se@NiTe$, pure NiTe, and RuO_2. This result ensures that the optimized $Ni_6Co_6Se@NiTe$ can efficiently catalyze urea molecules with lower kinetic barriers, consistent with the findings of LSV. The synergism and strong electron transfer between Ni and Co are more conducive to boosting the reaction kinetics.

To demonstrate the kinetics of UOR and oxygen evolution reaction (OER) process over the proposed $Ni_6Co_6Se@NiTe$ electrode, LSV profiles in 1 M KOH and 1 M KOH + 0.5 M urea are presented in Figure 5d. No electrocatalytic response can be realized in the case of using 0.5 M urea as the supporting electrolyte due to the blocking effect. On the other hand, a typical pre-oxidation reaction takes place before the OER process in a pure KOH solution. The oxidation peak of
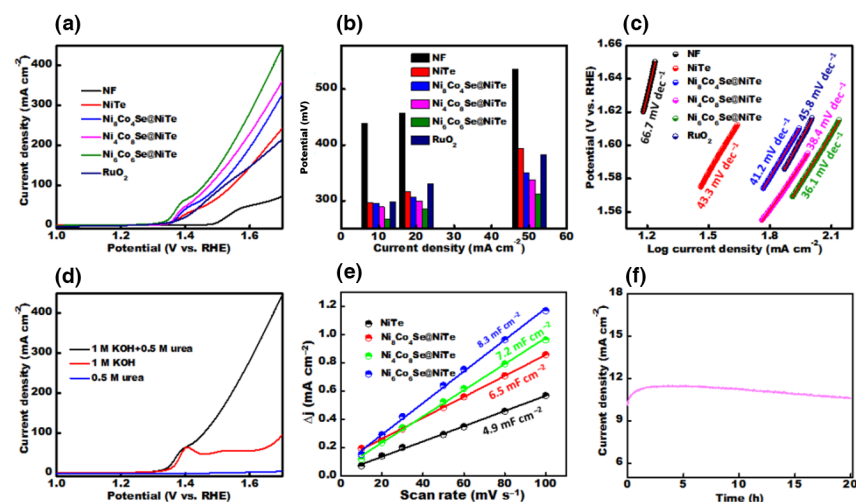
Figure 5. a) UOR polarization curves of target electrodes in 1 M KOH with 0.5 M urea at a scan rate of 5 mV s^{-1}, b) potentials of electrodes at 10, 20, and 50 mA cm^{-2}, c) Tafel plots, d) LSV curves of optimized Ni$_6$Co$_6$Se@NiTe electrode in 1.0 M KOH solution with and without 0.5 M urea at 5 mV s^{-1}, e) relationship between the current density and applied sweep rate, and f) i–t curve of optimized Ni$_6$Co$_6$Se@NiTe electrode at a potential of ~1.34 V.

a fixed potential of about 1.34 V versus RHE (Figure 5f). Almost no property degradation can be observed even after continuous catalysis for 20 h, proving the exceptional long-term durability of UOR. The reason for such enhanced stability can be ascribed to the stable structure and robust adhesion between the deposited electroactive layers and NF current collector (Supporting Information Figure S9). The direct growth of catalytic films on conductive scaffolds protects the active materials from being detached or even aggregated during prolonged catalysis processes, which presents an important issue for improving stability.

Field emission scanning electron microscope and TEM imagery recorded after the amperometric i–t stability test (Supporting Information Figures S10 and S11) indicate that the architectures and morphologies of the Ni$_6$Co$_6$Se@NiTe electrode are almost retained, implying the good structural stability. The highly open channels can effectively mitigate the huge accumulation of bubbles and accelerate their discharge from the electrode active surface. Additionally, after the long-term i–t stability test, XPS analysis was also performed, and the results are depicted in Supporting Information Figure S12.

Taking into account the excellent electrochemical characteristics of optimized Ni$_6$Co$_6$Se@NiTe toward UOR in an alkaline environment, the overall urea–water electrolysis system was implemented in a 1.0 M KOH aqueous solution with a two-electrode configuration using the same bifunctional electrode as both cathode and anode (**Figure 6**a). The entire Ni$_6$Co$_6$Se@NiTe ‖ Ni$_6$Co$_6$Se@NiTe electrolysis system demonstrates the superiority of anodic UOR compared to conventional water electrolysis. For comparison, commercial RuO$_2$ and Pt-C supported onto NF were also investigated to establish a urea electrolyzer in the alkali media, denoted as RuO$_2$@NF ‖ Pt-C/NF (+, −). The LSV polarization curves of Ni$_6$Co$_6$Se@NiTe ‖ Ni$_6$Co$_6$Se@NiTe cell for UOR+OER (1.0 M KOH + 0.5 M) and OER (1.0 M KOH) at a sweep rate of 5 mV s^{-1} are displayed in Figure 6b. Obtained results disclose the enhanced electrocatalytic properties of established Ni$_6$Co$_6$Se@NiTe ‖ Ni$_6$Co$_6$Se@NiTe electrolyzer for the overall urea-rich water electrolysis. The cell potential for overall water electrolysis in 1.0 M KOH solution directed by Ni$_6$Co$_6$Se@NiTe ‖ Ni$_6$Co$_6$Se@NiTe (Figure 6b)

and RuO$_2$@NF ‖ Pt-C/NF (Supporting Information Figure S13) couple to drive a current density of 10 mA cm^{-2} is 1.57 and 1.59 V, respectively. Whereas the overall urea electrolysis reaction in 1.0 M KOH with 0.5 M urea starts at 1.33 and 1.42 V for the Ni$_6$Co$_6$Se@NiTe ‖ - Ni$_6$Co$_6$Se@NiTe and RuO$_2$@NF ‖ Pt-C/NF cells and reaches 10 mA cm^{-2} at a potential of 1.38 and 1.49 V, respectively. This signifies that the Ni$_6$Co$_6$Se@NiTe ‖ Ni$_6$Co$_6$Se@NiTe device is a promising candidate for overall urea–water electrolysis in alkaline conditions. Alongside, the Ni$_6$Co$_6$Se@NiTe ‖ Ni$_6$Co$_6$Se@NiTe urea electrolyzer achieves 50 and 75 mA cm^{-2} at 1.58 and 1.64 V, respectively, which are ~150 and 261 mV lower than those for traditional water electrolysis (Figure 6b). The voltage difference between the UOR+OER and OER electrocatalysis reactions gradually expands with increasing the current density (Figure 6c). This substantiates that replacing the sluggish OER with the favorable UOR can markedly enhance the efficiency of H$_2$ generation. The validity of integrating the Ni$_6$Co$_6$Se@NiTe ‖ Ni$_6$Co$_6$Se@NiTe urea electrolyzer can be further evidenced by monitoring the catalytic efficacy at a high current density. Notably, the proposed cell requires a low cell potential of 1.69 V to deliver 100 mA cm^{-2} (Figure 6c). The electrocatalytic performance of our proposed Ni$_6$Co$_6$Se@NiTe ‖ Ni$_6$Co$_6$Se@NiTe electrolyzer toward overall UOR electrocatalysis is impressive and even exceeds other recently reported systems. Figure 6d illustrates the overpotentials required to attain a current density of 10 mA cm^{-2} for overall UOR.[39–49]

The finding drawn is that optimizing heterojunctions between Ni$_6$Co$_6$Se and NiTe can effectively regulate the synergistic effect between electrochemically active components and promote utilization efficiency. This binder-free heterostructured electrode with manipulated electronic structure and unique arrayed architecture exhibits high catalytic activity and durability for the UOR process. Furthermore, the long-term durability of the constructed cell was also tested in 1.0 M KOH with 0.5 M urea. Figure 6e depicts that the cell can maintain the current response almost at a constant level for 40 h, benefiting from the freestanding configuration and rich heterostructure interface. This result demonstrates that Ni$_6$Co$_6$Se@NiTe can serve as a stable electrode for overall urea–water electrolysis in alkaline media. Besides, the polarization curves for the Ni$_6$Co$_6$Se@NiTe ‖ Ni$_6$Co$_6$Se@NiTe cell before and after the stability test were recorded as displayed in Figure 6f. Observation indicates a very slight change in the cell voltage. The positive shift in the cell voltage is only ~10 mV at 10 mA cm^{-2}, manifesting the excellent stability of Ni$_6$Co$_6$Se@NiTe.

2.3. Supercapacitive Performances of Ni$_x$Co$_{12-x}$Se@NiTe Core–Shell Heterostructures

The electrochemical behaviors of freestanding Ni$_x$Co$_{12-x}$Se@NiTe core–shell heterostructures as positive electrodes were initially measured with a three-electrode setup into a 2.0 M KOH aqueous electrolyte. **Figure 7a** presents the CV profiles of as-prepared electrodes at 10 mV s^{-1} in the potential window of 0.05–0.55 V versus SCE. All the CV signals
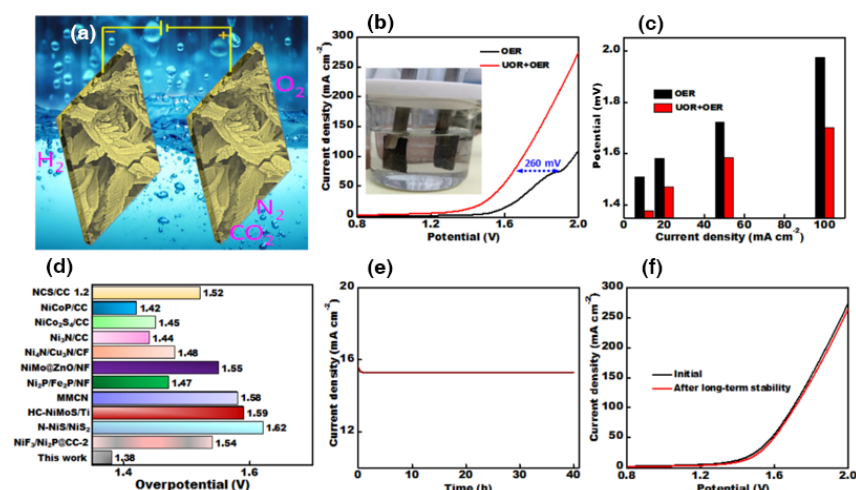
Figure 6. a) A schematic diagram of constructed electrolysis cell equipped with the bifunctional Ni$_6$Co$_6$Se@NiTe electrode as both cathode and anode, and b) linear sweep voltammetry curves of Ni$_6$Co$_6$Se@NiTe ‖ Ni$_6$Co$_6$Se@NiTe cell recorded in 1.0 M KOH electrolyte with and without 0.5 M urea at 5 mV s^{-1}. Inset depicts an optical image of the integrated system. c) Bar graph for the required potential at 10, 50, and 100 mA cm^{-2} with and without 0.5 M urea. d) The potential value of Ni$_6$Co$_6$Se@NiTe ‖ Ni$_6$Co$_6$Se@NiTe cell at 10 mA cm^{-2} compared with the presented cells in previous reports,[39–49] e) i–t response for the cell in 1.0 M KOH and 0.5 M urea electrolyte for 40 h at a constant potential of 1.46 V, and f) polarization curves of the cell at initial and after long-term stability test.
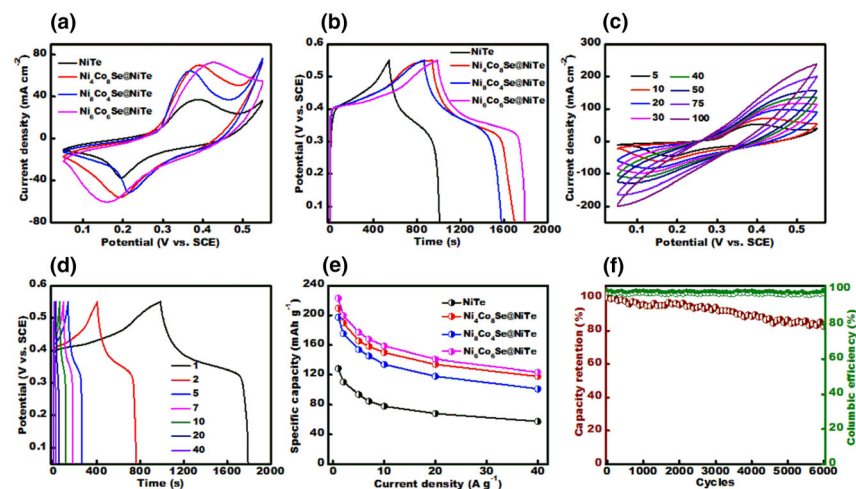

Figure 7. Electrochemical behaviors of NiTe and heterostructured Ni$_x$Co$_{12-x}$Se@NiTe core–shell electrodes obtained in 2.0 M KOH electrolyte with a three-electrode setup. a) CV curves at 10 mV s^{-1}, b) GCD curves at 1 A g^{-1}, c) CV profiles of optimized Ni$_6$Co$_6$Se@NiTe electrode at different sweep rates, d) GCD curves of Ni$_6$Co$_6$Se@NiTe electrode at different current densities, e) plots of specific capacity versus current density, and f) cyclic performance and capacity retention of Ni$_6$Co$_6$Se@NiTe electrode over 6000 GCD times at 20 A g^{-1}.

illustrate a couple of redox peaks, elucidating the battery-type-like behavior of electrodes controlled by the reversible Faradaic reactions of Ni^{2+}/Ni^{3+} and Co^{2+}/Co^{3+} ions during the electrochemical redox process. Importantly, the CV curve of the Ni$_6$Co$_6$Se@NiTe electrode reveals a higher peak current response and a larger integral area compared with other electrodes, certifying its exceptional specific capacity.

Next, the GCD measurements at a current density of 1 A g^{-1} were conducted on pure NiTe and Ni$_x$Co$_{12-x}$Se@NiTe core–shell electrodes within a potential range of 0.05–0.55 V versus SCE. To validate the

systematic role of deposited compositions and exclude the influence of the current collector, the capacitive behavior of the precleaned NF substrate was also evaluated under similar conditions and the resulting capacitance can be neglected compared with the target electrodes (Supporting Information Figure S14). Figure 7b shows the GCD curves of NiTe and Ni$_x$Co$_{12-x}$Se@NiTe electrodes obtained with obvious charge–discharge voltage platforms, consistent with the CV results. This observation confirms the Faradaic battery-type behavior of developed electrodes. All the core–shell-regulated electrodes display a longer discharge time than pure NiTe, which benefits from the established heterojunctions and manipulated electrochemical active sites. The good symmetrical GCD profiles signify the enhanced Coulombic efficiency and reversibility. Notably, the Ni$_6$Co$_6$Se@NiTe electrode has the longest discharge time compared with those of other electrodes, endorsing a higher specific capacity.

The CV curves of pure NiTe and Ni$_x$Co$_{12-x}$Se@NiTe core–shell electrodes at various sweep rates (5–100 mV s^{-1}) were collected as depicted in Figure 7c and Supporting Information Figure S15. With a 20-fold increment of applied sweep rate, the current response raises accordingly, suggesting prominent reversible Faradaic behaviors with tunable rate capability.[50] Furthermore, the oxidation and reduction peak positions gradually move toward the high and low potential, respectively, with increasing the sweep rate. This is caused by the charge diffusion polarization and influential impact of sweep rate on battery-type electrode material.[51] The linear correlation between peak current density and the square root of sweep rate verifies the occurrence of a diffusion-controlled process at the electrode/electrolyte interfaces (Supporting Information Figures S15 and S16). The diffusion coefficient of electrolytic OH$^-$ along structured Ni$_6$Co$_6$Se@NiTe electrode can be expressed by the Randles–Sevčik formula (Equation 1).[52,53]

$$i = 0.446\, nFC \left(\frac{nFvD}{RT} \right)^{0.5} \tag{1}$$

where i, n, F, C, v, D, R, and T are, respectively, the current density (A g^{-1}), number of exchanged electrons in an electrochemical reaction, Faraday constant (C mol^{-1}), electrolyte concentration (M), applied sweep rate (V s^{-1}), diffusion coefficient (cm^2 s^{-1}), universal gas constant (J K^{-1} mol^{-1}), and the reaction temperature (K). As can be seen, the diffusion coefficient linearly varies with v$^{1/2}$. On the basis of fitted lines, the diffusion coefficient of OH$^-$ anions into heterostructured Ni$_6$Co$_6$Se@NiTe electrode is estimated to be ~2.46 × 10^{-11} cm^2 s^{-1}, proving its good ability to shuttle electrolytic OH$^-$ ions into both surface and core layers. Furthermore,

the charge storage kinetics of an electrode is explored from the CV results. The logarithmic relationship between the peak current density and sweep rate (log I/log v) can be disclosed by the power law (Equation 2).[54]

$$i = av^b \tag{2}$$

both a and b are adjustable coefficients. The value of b can be derived from the slope of the linear log I/log v plot. A surface-controlled process-based capacitive-like performance is demonstrated with a b-value of 1, while a diffusion-controlled reaction exists with a b-value of 0.5. Apparently, the pure NiTe and $Ni_xCo_{12-x}Se@NiTe$ electrodes realize the b-value close to 0.5 for both oxidation and reduction peak current spectrum. This result indicates that the charge storage behavior of electrodes is dominated by a diffusion-controlled process (Supporting Information Figures S15 and S16).

The GCD patterns of pure NiTe and $Ni_xCo_{12-x}Se@NiTe$ core–shell electrodes under different current densities are presented in Figure 7d and Supporting Information Figure S17. Both charge and discharge platforms are shortened with increasing the current density, manifesting that the specific capacity is affected by the intercalation and de-intercalation mechanism of the Faradaic battery-type material. The specific capacities and rate performances of electrodes at various current densities from 1 to 40 A g^{-1} are computed from the discharge branches of obtained GCD profiles as displayed in Figure 7e. The $Ni_6Co_6Se@NiTe$ electrode achieves a higher specific capacity with an enhanced rate capability. The specific capacity of $Ni_6Co_6Se@NiTe$ electrode at 1, 2, 5, 7, 10, 20, and 40 A g^{-1} is 223, 199.7, 177.5, 168, 159, 141, and 123.7 mA h g^{-1}, respectively. On the contrary, the specific capacities of pure NiTe are 128.5, 102, 93.7, 84.7, 78, 68, and 57.4 mA h g^{-1} at similar current densities. The specific capacity of $Ni_8Co_4Se@NiTe$ and $Ni_4Co_8Se@NiTe$ at a current density of 1 A g^{-1} are 197.3 and 209 mA h g^{-1}, respectively. The NiTe, $Ni_8Co_4Se@NiTe$, $Ni_6Co_6Se@NiTe$, and $Ni_4Co_8Se@NiTe$ electrodes can retain about 44.7%, 51.2%, 55.5%, and 56.2% of the original capacity, respectively, at a higher current density of 40 A g^{-1}. The enhanced capacitive performance of the $Ni_6Co_6Se@NiTe$ electrode originates from the integrated Ni_6Co_6Se porous shell and effective synergism of all constituents, which not only increase the kinetics of Faradaic redox reactions and broaden the active contact area but afford rich heterojunctions. The porous characteristics of an electrode can offer several OH^- and mass transport channels. Thus, $Ni_6Co_6Se@NiTe$ is the optimized proportion taking all the above features together. The acquired specific capacity of the $Ni_6Co_6Se@NiTe$ core–shell electrode is considerably comparable to other transition metal electrodes reported in the literature, ensuring its remarkable charge storage capability (Supporting Information Table S2).

To study the inner electrochemical mechanism contributing to the charge storage process, EIS analysis was performed for pure NiTe and $Ni_xCo_{12-x}Se@NiTe$ core–shell electrodes. As shown in Supporting Information Figure S18A, the acquired Nyquist plots of target electrodes exhibit a similar pattern with a semicircle in the high-frequency part and a linear line in the low-frequency region. The semicircle represents the R_{ct} induced by the charge transfer process and electrolyte infiltration on both surface and bulk, while the liner section is attributed to the Warburg diffusion process in the bulk.[55] The simulated equivalent circuit was investigated to fit the Nyquist plots, where R_{ct}, R_s, CPE, and W constitute the charge transfer resistance, electrolyte resistance, constant phase element, and Warburg diffusion resistance,

respectively.[55,56] The smaller R_{ct} for the $Ni_xCo_{12-x}Se@NiTe$ hybrid should be ascribed to the chemical combination of $Ni_xCo_{12-x}Se$ with favorable synergism. Results manifest the $Ni_6Co_6Se@NiTe$ with the R_{ct} value of 1.46 Ω, which is obviously lower than that of pure NiTe (2.68 Ω). Additionally, the enhanced slopes of steep lines for $Ni_xCo_{12-x}Se@NiTe$-based electrodes indicate a rapid ion diffusion rate due to lower diffusion resistance along the 2D porous nanosheets and additional redox active sites induced by the Ni and Co ions on the shell. The Bode phase angle plot (Supporting Information Figure S18B) demonstrates an insignificant change in the negative phase angle values within the low- and high-mid-frequency domain, proposing that the developed electrodes attenuate the diffusion limitations.[57] However, the relaxation time constant ($\tau_0 = f_0^{-1}$, where f_0 denotes the knee frequency at a phase angle of 45°) for $Ni_xCo_{12-x}Se@NiTe$ is reduced compared to NiTe, implying a fast reaction rate and an enhanced charge transfer resistance. The relaxation time constant is measured to be 31.62, 21.54, 16.78, and 14.68 ms for NiTe, $Ni_8Co_4Se@NiTe$, $Ni_4Co_8Se@NiTe$, and $Ni_6Co_6Se@NiTe$, respectively. In sum, the EIS outcomes confirm that creating core–shell-like architectures diminishes the R_{ct} and modulates the ion diffusion kinetics as well, therefore contributing to the high specific capacitance of $Ni_xCo_{12-x}Se@NiTe$ hybrids.

The cycling performance of the as-fabricated $Ni_6Co_6Se@NiTe$ electrode was tested by GCD analysis. As presented in Figure 7f, about 82.6% of the initial capacity is maintained after continuous 6000 charge–discharge times at a high current density of 20 A g^{-1}, suggesting a good cycling characteristic. The $Ni_6Co_6Se@NiTe$ electrode exhibits a high Coulombic efficiency of 97.8% (Figure 7f), revealing good electrochemical stability. Low-resolution and magnified SEM images (Supporting Information Figure S19) after cyclic tests for 6000 GCD cycles confirm that the overall morphology still maintains a hierarchical framework without significant change in microstructure. This proves the stability and integrity of electrode structure in the alkaline medium. The composition and electronic properties of the $Ni_6Co_6Se@NiTe$ electrode after cyclic tests were also probed by XRD and XPS characterization (Supporting Information Figure S20). The core–shell architectures with numerous void spaces and channels can impressively store the electrolyte solution, significantly promote the charge transfer efficiency, and reinforce the rate performance. In addition, the larger ECSA is also an advantage contributing to the low diffusion resistance. The interconnected Ni_6Co_6Se nanosheet arrays may serve as an ion pool to speed up the ion transport rate and protect the core material during redox processes and continuous cycling tests.

2.3.1. Electrochemical Performances of $Ni_6Co_6Se@NiTe$//AC HASC Device

Aiming to investigate all the sustainable power sources with a large energy density and further assess the practicability of bifunctional $Ni_6Co_6Se@NiTe$ core–shell heterostructures, an aqueous HASC device was fabricated in 2.0 M KOH electrolyte by paring the battery-type $Ni_6Co_6Se@NiTe$ positive electrode and AC negative electrode with a filter paper as the separator (Supporting Information Figure S21). To balance the charge and identify the active mass of the positive and negative electrodes, the electrochemical and capacitive behaviors of AC/NF-based negative electrode were calculated in 2.0 M KOH electrolyte with a three-electrode cell by using CV and GCD tests in the potential window of −1.0 to 0.0 V versus SCE. The comparative CV and GCD profiles of $Ni_6Co_6Se@NiTe$ positive electrode and AC/NF negative
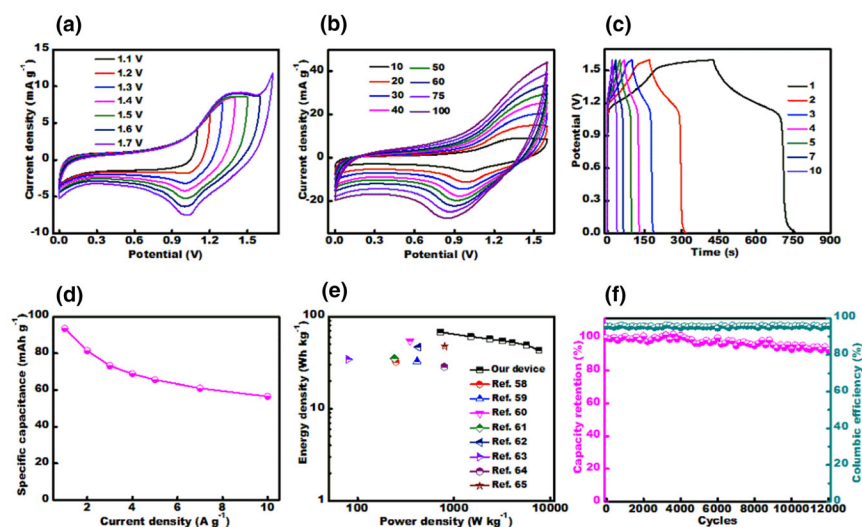
Figure 8. a) Cyclic voltammetry (CV) profiles of as-constructed $Ni_6Co_6Se@NiTe//AC$ device at various potential scans, b) CV curves at different sweep rates, c) GCD tests at various current densities, d) capacity value and rate capability as a function of current density, e) comparison of the Ragone plot for the proposed $Ni_6Co_6Se@NiTe//AC$ HASC device with those of others reported,[58–65] and f) cycling performance and Coulombic efficiency of Ni6Co6Se@NiTe//AC device at 5 A g^{-1}.

electrode at 10 mV s^{-1} and 1 A g^{-1} are displayed in Supporting Information Figures S22 and S23, respectively. The as-prepared AC/NF negative electrode reaches a specific capacitance of 163.2 F g^{-1} at a current density of 1 A g^{-1}. According to the matched CV curves (Supporting Information Figure S22) and GCD results at 1 A g^{-1} (Supporting Information Figure S23), the optimal mass ratio between AC and Ni_6Co_6-Se@NiTe with respect to the charge balance formula can be fixed as 4.9:1.

To determine the stable operating cell potential, the resultant Ni6Co6Se@NiTe//AC HASC device was investigated at various voltages. As illustrated in **Figure 8a**, the maximum working potential after a sequence of CV tests at 10 mV s^{-1} can approach 1.6 V without an obvious polarization effect. The CV curve enveloped area grows correspondingly without a notable distortion, manifesting that the stable operating potential window can be broadened to 0–1.6 V. Moreover, a bump occurs in the CV profile upon extending the operating voltage window up to 1.7 V, which may result from the irreversible hydrolytic reaction or oxygen evolution. Thus, the working potential of 1.6 V was employed as the cell potential to evaluate the overall charge storage characteristics. This result can also be affirmed by the GCD results shown in Supporting Information Figure S24. The assembled Ni_6Co_6-Se@NiTe//AC device with various potential windows at a constant current density of 1 A g^{-1} can reach a maximum potential of 1.6 V with a good Coulombic efficiency.

Figure 8b shows the CV curves of constructed $Ni_6Co_6Se@NiTe//$AC device within the voltage window of 0–1.6 V at different scanning rates (10–100 mV s^{-1}). The CV profiles preserve a similar nondistorted feature with obvious redox characteristics even at higher sweep rates, suggesting a desirable rate capability and strong contribution from the existing Faradaic redox reactions. Side-by-side, the current density increases with increasing the scan speed, revealing appropriate charge storage properties. Such observations imply that the double-layer capacitance effect of AC and battery-type/Faradaic behavior of $Ni_6Co_6Se@$-NiTe effectively contribute to the enhanced electrochemical

performance of the resulting device. GCD results collected with various current densities (1–10 A g^{-1}) possess apparent voltage plateaus, signifying a typical battery-type reaction with an excellent reversibility (Figure 8c). The corresponding specific capacity of the Ni_6Co_6-Se@NiTe//AC HASC device estimated from the harvested GCD results at different current densities is given in Figure 8d. Based on the discharge curve, the HASC cell delivers a high specific capacity of 93.4 mAh g^{-1} at a current density of 1 A g^{-1}. Even at a higher current density of 10 A g^{-1}, the cell is still capable of providing 55.8 mAh g^{-1}, illustrating a high-rate activity.

Figure 8f depicts the Ragone plot of the yielded energy and power densities for the fabricated $Ni_6Co_6Se@NiTe//AC$ HASC device compared with the others in the literature. With the increase in current density, the energy density decreases, whereas the power density gradually enhances. Notably, the cell reaches a maximum energy density of 67.7 Wh kg^{-1} and a power density of 724.8 W kg^{-1} at 1 A g^{-1}, while a high energy density of 42.9 Wh kg^{-1} can still be yielded with a large power density of 7612 W kg^{-1} at 10 A g^{-1}. The high energy storage outcomes compare favorably with most previously reported state-of-the-art HASC systems as shown in Figure 8e[58–65] and Supporting Information Table S3. Besides, the long-term cycle stability of the assembled cell was assessed by GCD tests at 5 A g^{-1} for successive 12 000 cycles as shown in Figure 8f. Impressively, the cell can keep around 92.4% of its original capacity with a high Coulombic efficiency of 95.5%, certifying its excellent electrochemical cyclic performance over a prolonged time period. These prominent storage characteristics make the heterostructured $Ni_6Co_6Se@NiTe$ core–shell electrode a powerful platform for high-performance supercapacitors.

Next, EIS tests were carried out to understand the change in the charge transfer process and internal resistance after 12 000 charge–discharge cycles. Nyquist plots are depicted in Supporting Information Figure S25A. The negligible change in the linear line slope after cyclic stability tests certifies the improved capacitive response. As can be observed, there is a slight increase in the R_{ct} value from 3.89 to 4.52 Ω after cycling. The dependence of phase angle on the frequency was analyzed as displayed in Supporting Information Figure S25B. The phase angle plot declares a slightly more negative value in the high-mid-frequency area. The relaxation time of fresh and consumed device is calculated as 17.78 and 26.1 ms, respectively. Although the relaxation time increases after the cyclic test, the change is still small, signifying that the integrity of the assembled device is well maintained after potential cycling.[66] It is thus evident from the Bode plot (Supporting Information Figure S25B) that the $Ni_6Co_6Se@NiTe$ positive electrode has a shorter ionic transport path with a low internal resistance and an enhanced electronic structure. To confirm the practical feasibility of constructed $Ni_6Co_6Se@NiTe//AC$ system, two hybrid devices were assembled and connected in series after being charged to light a red light-emitting diode (LED) (Supporting Information Figure S26). The aforementioned findings firmly elucidate that the $Ni_6Co_6Se@NiTe//AC$ device has potential electrochemical charge storage performances.

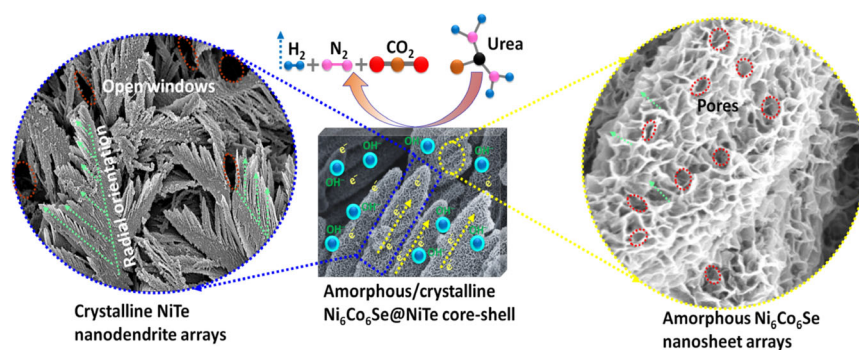**Figure 9.** Illustration for the systematic roles of bifunctional $Ni_6Co_6Se@NiTe$ core–shell heterostructures in overall urea electrocatalysis and supercapacitors.

Furthermore, the charge storage performance of the as-fabricated $Ni_6Co_6Se@NiTe//AC$ HASC device was calculated at 60 °C in 2.0 M KOH electrolyte (Supporting Information Figure S27). The GCD curves and the corresponding specific capacitance show an ideal battery-type/Faradaic redox charge storage behavior (Supporting Information Figure S27A). The cell approaches a maximum cell potential of 1.48 V and delivers a high specific capacity of 72.6 mAh g^{-1} at 1 A g^{-1} and maintains about ~53% of its original capacity at the higher current density of 10 A g^{-1} (Supporting Information Figure S27B). The Ragone plot is shown in Supporting Information Figure S27C with an energy density of 53.5 Wh kg^{-1} and a power density of 670.2 W kg^{-1}. A high-power density of 7008.6 W kg^{-1} can be yielded at a desirable energy density of 29.6 Wh kg^{-1}. The self-discharge performance of the $Ni_6Co_6Se@NiTe//AC$ HASC device was analyzed at a current density of 1 A g^{-1} at ~25 °C as indicated in Supporting Information Figure S27D. The open circuit voltage decay is a critical parameter to probe the self-discharge process of a supercapacitor. Before the test, the cell was charged/discharged at 1 A g^{-1} in the potential window from 0.0 to 1.6 V for 10 cycles. The open circuit voltage and voltage decay of the cell were recorded for 12 h. It decreases from 1.6 to ~0.69 V after 12 h, corresponding to a decay rate of 75.8 mV h^{-1}. Such result is comparable to those in literature.[67–70] Generally, self-discharge in a supercapacitor device can be induced by several reasons including diffusion-mediated pathways and overcharging issues.

2.4. Bifunctionality and Role of $Ni_6Co_6Se@NiTe$ Electrode for Overall Urea Electrocatalysis and Supercapacitors

Based on the enhanced electrocatalytic activity for UOR and overall urea electrolysis as well as the exceptional charge storage performance of bifunctional $Ni_6Co_6Se@NiTe$ core–shell heterostructures, the significant features and mechanisms inducing such a high electrochemical activity can be demonstrated as follows: the synergistic effect between 2D Ni_6Co_6Se nanosheet arrays and 3D NiTe dendritic frameworks with electron-rich Te and Se species and collaborative effects of Ni and Co electroactive sites and enlarged surface area effectively tune the overall electrochemical properties.[71,72] The direct deposition of active compounds onto conductive current collector improves the interfacial contact and mechanical adhesion between active components and underlying scaffolds and avoids the loss of electroconductivity and "dead volume" induced by the use of binder/additives.[73] Open dendritic frameworks of NiTe core and the highly porous nature of the

constructed shell with interconnected nanosheet networks afford enormous accessible centers for facile insertion/extraction of OH^- ions and strengthen the UOR as well as Faradaic redox processes.[74,75] These hierarchical open/porous architectures may serve as ion reservoirs/pools to create "expressways" for charge transfer and delivery and consequently accelerate the release of generated gas and bubbles. The core–shell heterostructures enlarge the interfacial contact area and offer easy penetration paths of ions/electrons inside the active material by utilizing both surface and interior as schematically illustrated in **Figure 9**.

The similar growth planes of core and shell along a vertical fashion promote the electrochemical stability during long-term operation without a significant structural distortion. Constructing a heterostructure between NiTe and Ni_6Co_6Se with rich heterojunctions may create lattice defects, benefit electron transfer efficiency, and expose more electrochemical active sites, thus greatly tuning the UOR activity and capacitive behavior. The co-existence of Te and Se with different electronegativity stabilizes the charge redistribution and modulates the absorption of OH^-.[60] Besides, both Te and Se atoms can delicately regulate the overall electron structure and adjust the binding energies of intermediates during the reaction process, enabling a high electrochemical activity. The internal electron transfer may optimize the binding energy of NiCo-Se/Ni–Te bonds and endow the quadruple hierarchy $Ni_6Co_6Se@NiTe$ with decent electrochemical stability. As a result, this study not only presents a low-cost and bifunctional core–shell heterostructured electrode with encouraging outcomes but also an efficient and feasible approach to exploring highly active materials with high performance for electrocatalytic applications and energy storage systems.

3. Conclusions

In summary, hierarchical porous $Ni_xCo_{12-x}Se@NiTe$ core–shell heterostructures as advanced binder-free configurations were fabricated via a two-step electrochemical deposition method and directly applied for electrocatalytic UOR and supercapacitors. More importantly, the core–shell synergistic modulation involving 3D NiTe dendritic frameworks and 2D $Ni_xCo_{12-x}Se$ nanosheets network not only maintains the structural stability and restrains the aggregation of building units but also improves the conductivity and boosts the electrochemical activity. The highly open architectures with a similar growth direction along the vertical axis expose multiple electroactive sites and diverse transport pores/channels for mass/electrons. Electrochemical tests reveal that the intimate combination of NiTe core and $Ni_xCo_{12-x}Se$ shell with a strong interfacial synergistic effect significantly boosts the intrinsic electrochemical properties due to rich heterointerfaces and maximized accessible active sites. The optimized bifunctional $Ni_6Co_6Se@NiTe$ electrode exhibits a high activity and durability for UOR in alkaline media. More notably, using this electrode as both anode and cathode for overall urea−water electrolysis yields a low cell potential of 1.38 and 1.58 V at a current density of 10 and 50 mA cm^{-2}, respectively. Moreover, the electrode maintains an exceptional stability even after long-term work for 40 h without an obvious activity attenuation. As a battery-type positive electrode, the $Ni_6Co_6Se@NiTe$ displays a high specific capacity of

223 mAh g^{-1} at 1 A g^{-1} with a desirable rate capability. The as-assembled Ni$_6$Co$_6$Se@NiTe//AC HASC device realizes an impressive specific energy density of 67.7 Wh kg^{-1} and a power density of 724.8 W kg^{-1} together with an outstanding cyclic stability (92.4% capacity retention after 12 000 cycles). Benefiting from these attributes, the obtained Ni$_6$Co$_6$Se@NiTe core–shell heterostructures provide a model of the heterointerface engineering of materials with desired electrochemical activity and favorable stability for high-performance energy conversion and storage applications.

4. Experimental Section

Detailed information related to the synthesis of active electrodes, physicochemical characterization, and electrochemical evaluation of bifunctional electrodes toward UOR and supercapacitor applications is provided in Supporting Information.

Acknowledgements

Conflict of Interest

The authors declare no conflict of interest.

Supporting Information

Supporting Information is available from the Wiley Online Library or from the author.

Keywords

[1] Y. G. Wang, Y. F. Song, Y. Y. Xia, *Chem. Soc. Rev.* **2016**, *45*, 5925.
[2] Y. Zhang, T. T. Zuo, J. Popovic, K. Lim, Y. X. Yin, J. Maier, Y. G. Guo, *Mater. Today* **2020**, *33*, 56.
[3] J. Wang, L. Han, B. Huang, Q. Shao, H. L. Xin, X. Huang, *Nat. Commun.* **2019**, *10*, 5692.
[4] D. Khalafallah, C. Ouyang, M. Zhi, Z. Hong, *Nanotechnology* **2020**, *31*, 475401.
[5] P. Simon, Y. Gogotsi, B. Dunn, *Science* **2014**, *343*, 1210.
[6] D. Khalafallah, M. Zhi, Z. Hong, *ChemCatChem* **2021**, *13*, 81.
[7] D. Khalafallah, M. Zhi, Z. Hong, *Top. Curr. Chem.* **2019**, *377*, 29.
[8] A. Noori, M. F. El-Kady, M. S. Rahmanifar, R. B. Kaner, M. F. Mousavi, *Chem. Soc. Rev.* **2019**, *48*, 1272.
[9] D. Khalafallah, Q. Zou, M. Zhi, Z. Hong, *Electrochim. Acta* **2020**, *350*, 136399.
[10] X. Sun, R. Ding, *Catal. Sci. Technol.* **2020**, *10*, 1567.
[11] D. Khalafallah, L. Xiaoyu, M. Zhi, Z. Hong, *ChemElectroChem* **2020**, *7*, 163.
[12] W. Choi, N. Choudhary, G. H. Han, J. Park, D. Akinwande, Y. H. Lee, *Mater. Today* **2017**, *20*, 116.
[13] E. T. Sayed, M. A. Abdelkareem, A. Bahaa, T. Eisa, H. Alawadhi, S. Al-Asheh, K.-J. Chae, A. G. Olabi, *Renew. Sust. Energ. Rev.* **2021**, *150*, 111470.
[14] H. Yuan, L. Kong, T. Li, Q. Zhang, *Chin. Chem. Lett.* **2017**, *28*, 2180.
[15] S. Zhang, D. Yang, M. Zhang, Y. Liu, T. Xu, J. Yang, Z.-Z. Yu, *Inorg. Chem. Front.* **2020**, *7*, 477.
[16] M.-R. Gao, Y.-F. Xu, J. Jiang, S.-H. Yu, *Chem. Soc. Rev.* **2013**, *42*, 2986.
[17] S. Ni, H. Qu, Z. Xu, X. Zhu, H. Xing, L. Wang, J. Yu, H. Liu, C. Chen, L. Yang, *Appl. Catal. B Environ.* **2021**, *299*, 120638.
[18] U. De Silva, J. Masud, N. Zhang, Y. Hong, W. P. R. Liyanage, M. A. Zaeem, M. Nath, *J. Mater. Chem. A* **2018**, *6*, 7608.
[19] Y. Qi, Z. Yang, S. Peng, M. Wang, J. Bai, H. Li, D. Xiong, *Inorg. Chem. Front.* **2021**, *8*, 4247.
[20] D. Khalafallah, C. Ouyang, M. Zhi, Z. Hong, *ChemElectroChem* **2019**, *6*, 5191.
[21] Y. Zhou, Y. Chen, M. Wei, H. Fan, X. Liu, Q. Liu, Y. Liu, J. Cao, L. Yang, *CrystEngComm* **2021**, *23*, 69.
[22] D. Khalafallah, Z. Wu, M. Zhi, Z. Hong, *Chem. Eur. J.* **2020**, *26*, 2251.
[23] S. Goriparti, E. Miele, F. De Angelis, E. Di Fabrizio, R. Proietti Zaccaria, C. Capiglia, *J. Power Sources* **2014**, *257*, 421.
[24] D. Khalafallah, X. Quan, C. Ouyang, M. Zhi, Z. Hong, *Renew. Energ.* **2021**, *170*, 60.
[25] D. Khalafallah, M. Zhi, Z. Hong, *J. Colloid Interface Sci.* **2022**, *606*, 1352.
[26] B. Ramulu, G. Nagaraju, S. C. Sekhar, S. K. Hussain, D. Narsimulu, J. Su Yu, *ACS Appl. Mater. Interfaces* **2019**, *11*, 41245.
[27] G. Qian, J. Chen, T. Yu, L. Luo, S. Yin, *Nano Micro Lett.* **2021**, *13*, 77.
[28] J. Xiao, H. Tong, F. Jin, D. Gong, X. Chen, Y. Wu, Y. Zhou, L. Shen, X. Zhang, *J. Power Sources* **2022**, *518*, 230763.
[29] H. Sun, Z. Yan, F. Liu, W. Xu, F. Cheng, J. Chen, *Adv. Mater.* **2020**, *3*, 1806326.
[30] L. Zhang, X. Zhao, W. Ma, M. Wu, N. Qian, W. Lu, *CrystEngComm* **2013**, *15*, 1389.
[31] J. Cao, K. Wang, J. Chen, C. Lei, B. Yang, Z. Li, L. Lei, Y. Hou, K. Ostrikov, *Nano Micro Lett.* **2019**, *11*, 67.
[32] L. Zhang, W. Chen, T. Wang, Y. Li, C. Ma, Y. Zheng, J. Gong, *Inorg. Chem. Front.* **2021**, *8*, 3230.
[33] Y.-Y. Sun, M.-Y. Jiang, L.-K. Wu, G.-Y. Hou, Y.-P. Tang, M. Liu, *Sustain. Energy Fuels* **2020**, *4*, 582.
[34] J. Chen, J. J. Davies, A. S. Goodfellow, S. M. D. Hall, H. G. Lancaster, X. Liu, C. J. Rhodes, W. Zhou, *Prog. Nat. Sci. Mater. Int.* **2021**, *31*, 141.
[35] X. Zheng, J. Jiang, T. Bi, F. Jin, M. Li, *ACS Appl. Energy Mater.* **2021**, *4*, 3288.
[36] Z. Ji, Y. Song, S. Zhao, Y. Li, J. Liu, W. Hu, *ACS Catal.* **2022**, *12*, 569.
[37] S. Adhikari, S. Kwon, D.-H. Kim, *Chem. Eng. J.* **2020**, *402*, 126192.
[38] Y. Li, H. Jiang, Z. Cui, S. Zhu, Z. Li, S. Wu, L. Ma, X. Han, Y. Liang, *J. Phys. Chem. C* **2021**, *125*, 9190.
[39] K. Wang, W. Huang, Q. Cao, Y. Zhao, X. Sun, R. Ding, W. Lin, E. Liu, P. Gao, *Chem. Eng. J.* **2022**, *427*, 130865.
[40] H. Liu, Z. Liu, F. Wang, L. Feng, *Chem. Eng. J.* **2020**, *397*, 125507.
[41] X. Wang, J. Wang, X. Sun, S. Wei, L. Cui, W. Yang, J. Liu, *Nano Res.* **2018**, *11*, 988.
[42] C. Xiao, S. Li, X. Zhang, D. R. MacFarlane, *J. Mater. Chem. A* **2017**, *5*, 7825.
[43] L. Yan, L. Sun, E. Hu, J. Ning, Y. Zhong, Z. Zhang, Y. Hu, *J. Colloid Interface Sci.* **2019**, *541*, 279.
[44] J. Cao, H. Li, R. Zhu, L. Ma, K. Zhou, Q. Wei, F. Luo, *J. Alloys Compd.* **2020**, *844*, 155382.
[45] J. Li, C. Yao, X. Kong, Z. Li, M. Jiang, F. Zhang, X. Lei, *ACS Sustain. Chem. Eng.* **2019**, *7*, 13278.
[46] Q. Liu, L. Xie, F. Qu, Z. Liu, G. Du, A. M. Asiri, X. Sun, *Inorg. Chem. Front.* **2017**, *4*, 1120.
[47] W. Zhu, M. Ren, N. Hu, W. Zhang, Z. Luo, R. Wang, J. Wang, L. Huang, Y. Suo, J. Wang, *ACS Sustain. Chem. Eng.* **2018**, *6*, 5011.

[48] L. Sha, J. Yin, K. Ye, G. Wang, K. Zhu, K. Cheng, J. Yan, G. Wang, D. Cao, *J. Mater. Chem. A* **2019**, 7, 9078.

[49] P. Hao, W. Zhu, L. Li, J. Tian, J. Xie, F. Lei, G. Cui, Y. Zhang, B. Tang, *Electrochim. Acta* **2020**, 338, 135883.

[50] B. Huang, W. Wang, T. Pu, J. Li, C. Zhao, L. Xie, L. Chen, *Chem. Eng. J.* **2019**, 375, 121969.

[51] J. Ma, J. Xia, Z. Liang, X. Chen, Y. Du, C.-H. Yan, *Small* **2021**, 17, 2104423.

[52] T. Nguyen, M. Fátima Montemor, *J. Mater. Chem. A* **2018**, 6, 2612.

[53] Y. Li, B. Huang, X. Zhao, Z. Luo, S. Liang, H. Qin, L. Chen, *J. Power Sources* **2022**, 527, 231149.

[54] D. Khalafallah, X. Li, M. Zhi, Z. Hong, *ACS Appl. Nano Mater.* **2021**, 4, 14258.

[55] F. B. M. Ahmed, D. Khalafallah, M. Zhi, Z. Hong, *Adv. Compos Hybrid Mater.* **2022**, 5, 2500.

[56] D. Khalafallah, M. Zhi, Z. Hong, *Ceram. Int.* **2021**, 47, 29081.

[57] N. M. Santhosh, K. K. Upadhyay, P. Stražar, G. Filipič, J. Zavašnik, A. M. Ferro, R. P. Silva, E. Tatarova, M. F. Montemor, U. Cvelbar, *ACS Appl. Mater. Interfaces* **2021**, 13, 20559.

[58] N. R. Chodankar, S. J. Patil, S.-K. Hwang, P. A. Shinde, S. V. Karekar, G. S. R. Raju, K. S. Ranjith, A. G. Olabi, D. P. Dubal, Y. S. Huh, Y.-K. Han, *Energy Stor. Mater.* **2022**, 49, 564.

[59] H. Peng, J. Zhou, K. Sun, G. Ma, Z. Zhang, E. Feng, Z. Lei, *ACS Sustain. Chem. Eng.* **2017**, 5, 5951.

[60] A. Gopalakrishnan, S. Badhulika, *Energy Fuel* **2021**, 35, 9646.

[61] Q. Hu, X. Jiang, M. He, Q. Zheng, K. H. Lam, D. Lin, *Electrochim. Acta* **2020**, 338, 135896.

[62] J. Yu, D. Yao, Z. Wu, G. Li, J. Song, H. Shen, X. Yang, W. Lei, F. Wu, Q. Hao, *ACS Appl. Energy Mater.* **2021**, 4, 3093.

[63] L. Han, P. Tang, L. Zhang, *Nano Energy* **2014**, 7, 42.

[64] L. Lin, L. Li, S. Hussain, S. Zhao, L. Wu, X. Peng, N. Hu, *Appl. Surf. Sci.* **2018**, 452, 113.

[65] Y. Huang, S. Ge, X. Chen, Z. Xiang, X. Zhang, R. Zhang, Y. Cui, *Chem. Eur. J.* **2019**, 25, 14117.

[66] T. Purkait, G. Singh, D. Kumar, M. Singh, R. S. Dey, *Sci. Rep.* **2018**, 8, 640.

[67] M. M. Ovhal, N. Kumar, S. K. Hong, H. W. Lee, J. W. Kang, *J. Alloys Comp.* **2020**, 828, 154447.

[68] W. Zhang, W. Yang, H. Zhou, Z. Zhang, M. Zhao, Q. Liu, J. Yang, X. Lu, *Electrochim. Acta* **2020**, 357, 136855.

[69] J. Wang, B. Ding, X. Hao, Y. Xu, Y. Wang, L. Shen, H. Dou, X. Zhang, *Carbon* **2016**, 102, 255.

[70] T. Tevi, H. Yaghoubi, J. Wang, A. Takshi, *J. Power Sources* **2013**, 241, 589.

[71] D. Guo, Y. Zhang, W. Sun, W. Chu, B. Li, L. Tan, H. Ma, H. Pang, X. Wang, L. Zhang, *ACS Appl. Mater. Interfaces* **2019**, 11, 41580.

[72] L. Liu, X. Yu, W. Zhang, Q. Lv, L. Hou, Y. Fautrelle, Z. Ren, G. Cao, X. Lu, X. Li, *ACS Appl. Mater. Interfaces* **2022**, 14, 2782.

[73] D. Khalafallah, J. Miao, M. Zhi, Z. Hong, *Appl. Surf. Sci.* **2021**, 564, 150449.

[74] R. Bai, X. Luo, D. Zhen, C. Ci, J. Zhang, D. Wu, M. Cao, Y. Liu, *Int. J. Hydrog. Energy* **2020**, 45, 32343.

[75] D. Khalafallah, W. Huang, M. Wunn, M. Zhi, Z. Hong, *J. Energy Storage* **2022**, 45, 103716.